Earth Planet. Sci. Lett. 663 (2025) 119416

Contents lists available at ScienceDirect

Earth and Planetary Science Letters

journal homepage: www.elsevier.com/locate/epsl

Sound velocity measurements of γ-$(Mg_{0.91}Fe_{0.09})_2SiO_4$ show that the ringwoodite to bridgmanite and ferropericlase phase transformation does not produce the seismically observed 660 km discontinuity

Rong Huang [a,b,*], Andrew R. Thomson [a,c,d], John P. Brodholt [a,e], Wilson A. Crichton [c], Anja Rosenthal [c,f], Dmitrii Druzhbin [c], Nicholas Backhouse [a], Isaac Taschimowitz [a], Dimitrios Bessas [c], Sergey Yaroslavtsev [c], Biao Wang [g]

[a] Department of Earth Sciences, University College London, London, UK
[b] Department of Earth and Environmental Sciences, University of Michigan, Ann Arbor, MI, 48109, USA
[c] ESRF – The European Synchrotron, Grenoble, France
[d] Natural History Museum, London, SW7 5BD, UK
[e] Center for Planetary Habitability, University of Oslo, Oslo, Norway
[f] Research School of Earth Sciences, Australian National University, Canberra, Australia
[g] Department of Earth Sciences, University of Oxford, Oxford, UK

ARTICLE INFO

Editor: Dr J Badro

Keywords:
Ringwoodite
Sound velocity
Ultrasonic interferometry
Mantle transition zone
660-km discontinuity
Pyrolite
Seismic reference model

ABSTRACT

The canonical model of Earth's interior directly links the global 410 and 660 km seismic discontinuities to olivine's high pressure phase transitions in a pyrolite mineral assemblage. However, previous studies observe that the expected sound velocities of pyrolite are too low to match 1-dimensional seismic models in the lower mantle transition zone (MTZ). In this study, we report measurements of the elastic properties of $(Mg_{0.9}Fe_{0.1})_2SiO_4$ ringwoodite (Rw90), the dominant component of pyrolite between 520 km and 660 km depths, using pulse-echo ultrasonic interferometry combined with synchrotron X-radiation in the multi-anvil press up to 21 GPa and 1650 K. Our results show that V_P and V_S of anhydrous Rw90 (0.003–0.035 wt.% H_2O, 5.6 ± 1.2% Fe^{3+}/Fe^{tot}) are both higher than predictions at MTZ conditions from previous studies, with a smaller increase for V_S. Simultaneous fitting of *PVT*-V_P-V_S data yields global fit equation of state (EoS) parameters of V_0= 39.69(2) cm^3/mol, K_0 = 183 (4) GPa, K_0' = 5.5(3), G_0 = 125(2) GPa, G_0' = 1.3(1), q_0 = 0.3(3), γ_0 = 1.27(4), θ_0 = 1100(100) K and η_{S0} = 3.5 (2). Combining results with literature data, our predicted V_S for pyrolite produces a sharp discontinuity consistent with seismic models, although V_S is slightly lower than observed in the lower MTZ. In contrast, we find that pyrolite would not produce a large and sharp V_P discontinuity at 660 km as the jump in V_P caused by the decomposition of Rw90 is too small. A homogenous assemblage of pyrolite cannot, therefore, currently explain the seismic features in the lower MTZ. We also find that neither an accumulation of harzburgite nor basaltic crust immediately above or below the 660 km discontinuity explains the observations. Instead, either a heterogeneous mixture of some other chemically distinctive components is required or more prosaically, the elastic properties of all the other mantle phases need reevaluation.

1. Introduction

Pyrolite, a hypothetical rock composition constructed by combining mantle-derived magma (basalt) with the mantle-melt residue (harzburgite or dunite) in specified proportions, is widely accepted as representative of Earth's upper mantle (Ringwood, 1991). Based on laboratory measurements of phase relations and sound velocities of corresponding minerals, the predicted sound velocities of pyrolite agree well with geophysical observations of the MTZ down to 520 km (Irifune et al., 2008), as well as the top of the lower mantle down to 1200 km (Kurnosov et al., 2017). However, within the lowermost 150 km of the MTZ the velocities of pyrolite are lower than those typical of seismological models such as PREM (Dziewonski and Anderson, 1981) and AK135 (Kennett et al., 1995), and do not match the seismic velocity

* Corresponding author.
E-mail address: Rong.Huang@ucl.ac.uk (R. Huang).

https://doi.org/10.1016/j.epsl.2025.119416
Received 7 October 2024; Received in revised form 30 April 2025; Accepted 2 May 2025
Available online 15 May 2025

jump at the 660 km (Gréaux et al., 2019; Irifune et al., 2008; Pamato et al., 2016; Xu et al., 2008). As such, various hypotheses have been proposed to reconcile seismology with an overall pyrolitic composition mantle, including the enrichment of harzburgite-rich or basalt-rich materials in the MTZ (Gréaux et al., 2019; Pamato et al., 2016; Yu et al., 2023).

However, accurate interpretation of seismic profiles in terms of mantle mineralogy and chemistry requires precise elasticity data of candidate minerals under relevant mantle conditions. The thermo-elastic properties of Rw90, which constitutes 60 vol.% of pyrolite between depths of 520 and 660 km, have previously been investigated through high-pressure experiments in diamond anvil cell (DAC) and multi-anvil apparatus (MA), in combination with various methods such as ultrasonic interferometry (*e.g.* Higo et al., 2008, 2006; Jacobsen and Smyth, 2006; Jacobsen et al., 2004), ultrasonic resonance (*e.g.* Mayama et al., 2005), and Brillouin scattering techniques (*e.g.* Mao et al., 2012; Schulze et al., 2018; Sinogeikin et al., 2003; Zhou et al., 2022). However, most of these measurements were conducted at relatively low temperatures that are more than 1000 K below those expected at MTZ conditions (~1700–1900 K). This requires, therefore, the use of EoS extrapolations to predict sound velocities at appropriate MTZ conditions which can potentially introduce considerable uncertainties. To date, only a single study (Higo et al., 2008) has measured the sound velocity of Rw90 at high pressures and temperatures exceeding 1500 K. Furthermore, the volumes of nominally dry Rw90 have never been measured at high pressure with angle dispersive X-ray diffraction under hydrostatic conditions, even at room temperature, despite extensive discussions on the effects of water and Fe content on the elasticity of ringwoodite (Rw). As the MTZ is a potential water reservoir due to the high solubility of water in wadsleyite and Rw (2–3 wt.%, Fei and Katsura, 2020, 2021; Inoue et al., 2010; Smyth et al., 2003), establishing a reliable benchmark for dry Rw90 would enable us to quantitatively resolve existing discrepancies regarding the compositional and thermal effects on the sound velocities of Rw as well as the depths and magnitudes of discontinuities (Houser, 2016; Meier et al., 2009; Suetsugu et al., 2010, 2006; Van der Meijde et al., 2003).

Here we report simultaneous measurements of density, compressional and shear wave velocity of nominally dry polycrystalline Rw90 samples that extend to 21 GPa and 1650 K, using ultrasonic interferometry in a synchrotron-based multi-anvil press. The resulting data are fitted to a self-consistent thermo-elastic model to estimate the thermodynamic properties of Rw90, with statistically meaningful uncertainty estimates, across a range of pressure and temperature (*P-T*) conditions. Finally, we combine our results with existing thermodynamic models for other minerals to estimate the sound velocities of pyrolite and harzburgite assemblages along a typical mantle geotherm at the base of the Earth's MTZ, facilitating comparison with 1-dimensional seismic reference models.

2. Experiments

Polycrystalline Rw90 was made by hot-pressing San Carlos olivine at 20 GPa and 1673 K for 3 hours using a 1000-ton Walker-type multi-anvil press at University College London. The San Carlos olivine was initially ground into a fine powder (5–10 μm) in ethanol and then dried overnight in a vacuum oven (< 2 mbar) at 125 °C before being loaded into Re foil capsules. Two capsules, each with a diameter of 1.4 mm and a length of 1.5 mm, were loaded into the same assembly. 10 mm edge-length CoO-doped semi-sintered MgO octahedron with $LaCrO_3$ furnaces were employed with 4 mm edge-length truncated tungsten carbide cubes (a so-called 10/4 assembly) to generate high pressure conditions. Temperature was monitored with a type D thermocouple inserted longitudinally through the wall of the furnace, with the hot junction set at the center of the furnace between the two capsules.

The synthesis products were characterized using several techniques, including powder X-ray diffraction (XRD, λ = 1.78897 Å), scanning electron microscopy (SEM) combined with energy-dispersive spectroscopy (EDS), Fourier transform infrared spectroscopy (FTIR), and Mössbauer spectroscopy. Unpolarized FTIR spectra were recorded in transmission mode using a Thermo Scientific iN10 MX. FTIR measurements were performed through a portion of the sample which was doubly polished to a thickness of 228(1) μm and measured through a CaF_2 substrate over the spectral range of 950 to 6500 cm^{-1}. These analyses confirm that the samples were pure and nominally dry Rw, with an average chemical composition of $(Mg_{0.91}Fe_{0.09})_2SiO_4$ and a water content of 0.003–0.035 wt.% (Fig. S1). The reported range of sample water contents encompasses the upper and lower bound of uncertainty associated with FTIR spectra background subtraction. At ambient conditions, the unit-cell parameters of Rw90 were determined to be a = 8.07767(3) Å and V_0 = 527.057(6) $Å^3$. Mössbauer spectroscopy constrained the sample to have an $Fe^{3+}/\sum Fe$ ratio of 5.6 ± 1.2%, where the reported uncertainty is assessed based on variation between multiple fitting models (Fig. S2, see Text S1 for details). The Mössbauer spectrum, measured at room temperature in constant acceleration mode at the revived conventional Mössbauer laboratory adjoined to ID14 of the European Synchrotron Radiation Facility, was fitted using SYNCmoss (Yaroslavtsev, 2023). To prepare for ultrasonic measurements, after characterisation the sample was manipulated into fully dense cylinders with a diameter of 1.0 mm and length of ~0.55 mm, with both ends mirror polished.

Combined *in situ* X-ray and ultrasonic measurements were conducted at the ID06-LVP beamline of the European Synchrotron Radiation Facility (Crichton et al., 2024). A 10/4 assembly was again employed with a TiC + MgO composite furnace (Xu et al., 2020), and a schematic illustration of the cell assemblage is provided in Fig. S3. One end of the sample was in direct contact with a very finely double-polished alumina buffer rod while the other end was backed by a NaCl + MgO disk to maintain hydrostatic conditions, with NaCl also serving as the pressure marker. Gold foils (1 μm thick) were placed at both ends of the sample for length measurements via X-ray radiography, and an additional gold foil was inserted between the cube and buffer rod to enhance mechanical coupling for ultrasonic transmission. To improve X-ray transparency along the beam path, conventional ceramic materials were replaced with amorphous SiBCN(O) windows. The temperature was monitored using a $W_{97}Re_3$ –$W_{75}Re_{25}$ thermocouple, with the hot junction positioned within the NaCl + MgO disk.

Monochromatic synchrotron X-rays (λ = 0.2339 Å) were used to collect diffraction data on a 2D PILATUS3X-CdTe detector (Crichton et al., 2023) (Fig. S4). The sample−detector geometry was calibrated using an aliquot of the NIST SRM660a LaB_6 standard material. XRD data for both the sample and pressure marker were acquired continuously throughout the experiments at 3 s intervals during heating and 30 s intervals during ambient temperature compression or decompression. The diffraction images were integrated to one dimensional XRD patterns using the Dioptas software (Prescher and Prakapenka, 2015) and the unit-cell parameters of the sample and NaCl pressure calibrant were determined by batch Rietveld refinements using the GSAS-II software (Toby and Von Dreele, 2013). Experimental pressures were evaluated from the unit-cell volumes of NaCl using a cross-calibrated high-temperature EoS (Dorogokupets and Dewaele, 2007).

The sample lengths were determined by measuring the distance between the two gold marker foils at either end of the sample in X-ray radiographic images (Fig. S5). Absorption intensities within the radiographs were extracted along perpendicular profiles using the ImageJ software (Collins, 2007), with uncertainties in measured lengths typically being 3 pixels. The conversion factor between image pixels and actual lengths (1 pixel = 1.014(2) microns) was determined by comparing the measured lengths of samples and calibration objects, obtained with a digital gauge (±1 μm accuracy), to their corresponding image pixels from images taken in air, under slight compression (<< 1 GPa), or in complete decompression across multiple experiments (Fig. S6).

Ultrasonic waves were generated and received by a dual-mode 10° Y-cut $LiNbO_3$ piezoelectric transducer mounted with Epotek 353ND on the corner of the cube diagonally opposite to the anvil-buffer rod interface. Bursts of three consecutive sine waves with frequencies of 30–60 MHz were generated and transmitted to the transducer and oscilloscope by a waveform generator (Keysight 33622A). The reflected echoes were then recorded with a digital oscilloscope (Keysight DSOX4104). Two-way travel times of the P (50 MHz) and S (40 MHz) waves were determined using the 'pulse-echo overlap' method, by cross-correlating reflected signals from the top and bottom interfaces of the sample until they overlap (Fig. S7–S8). The travel time was corrected for the bond (gold foils) phase shift effect following the procedures of Noda et al. (2022). The final results of the P and S wave travel times are given in Table S1. The uncertainty on the travel-time is typically 0.2%, but the overall uncertainties in the velocity measurements are dominated by contributions from sample length measurements, which are ~0.7%. The combined uncertainties in reported velocities are ~0.8%.

Results from two experiments on samples of Rw90 composition are presented here. In the first run (ES1212-run4), the sample was initially compressed at room temperature to a target pressure of ~20 GPa and then heated to ~1000 K to reduce any non-hydrostatic stress. Ultrasonic data were then collected during subsequent heating and cooling ramps in steps of 100 or 200 K. Pressure was subsequently increased in steps of ~1–1.5 GPa and the same procedure was followed. Further measurements were also made during the release of pressure, encompassing three heating cycles up to 873 K. Unfortunately, during this process, the sample transformed back to olivine at ~6.4 GPa and 873 K. The *P-T* path of the entire experiment is shown in Fig. S9. In the second run (ES1135-run3), only *PVT* data were collected up to 20.7 GPa and 1478 K due to the weak ultrasonic signal, following the same procedure as above. Heating failed during the second heating cycle at ~20.6 GPa and 1443 K where the power became uncontrollable and data after this point were not used. Although XRD data were collected continuously during the two experiments, only data collected after heating to 1000 K when all stress is assumed to have relaxed have been used in fitting the EoS of Rw90 (Table S2–S3).

3. Results

3.1. Elasticity of nominally dry Fe-bearing Rw at high P-T conditions

Ultrasonic echo signals for both P- and S- waves were clearly observed throughout the entire experiment, with stacked spectra of these data shown in Fig. S7–S8. The molar volumes and sound velocities of Rw90 at high *P-T* conditions are plotted in Fig. 1(a)–(c) as a function of pressure, with the data colored by temperature. P- and S- wave velocities increase with increasing pressure and decrease with increasing temperature, as is typical for most minerals. V_P shows a greater pressure dependence, 0.056 km·s^{-1}·GPa^{-1} at 300 K, than V_S, 0.008 km·s^{-1}·GPa^{-1}. The temperature dependence is nonlinear for both V_P and V_S, becoming increasingly pronounced with increasing temperature. Data below 9.5 GPa are not plotted due to a small blow-out that occurred during decompression, just before the sample transformed back to olivine at ~6.5 GPa and 873 K, causing these data to deviate from the overall

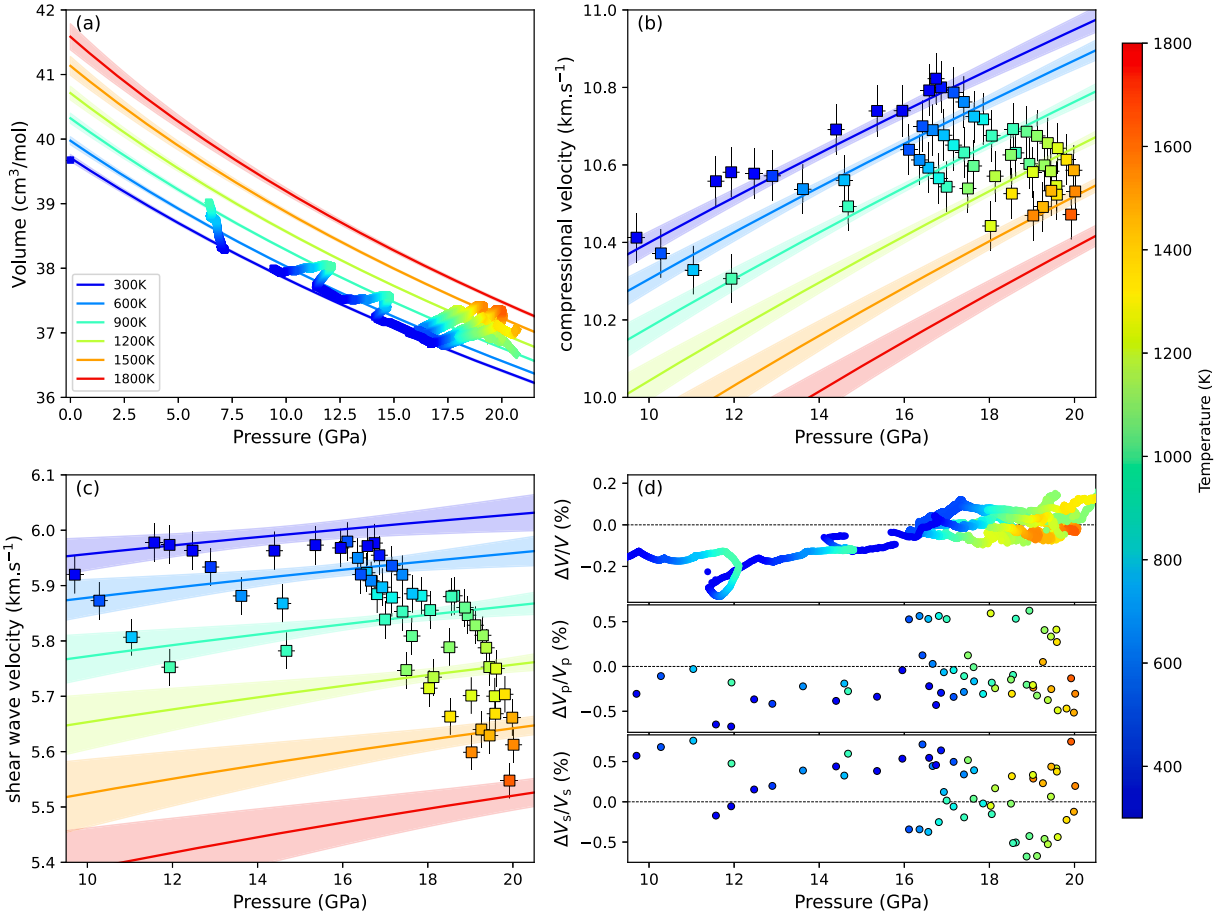

Fig. 1. (a) Volume (V), (b) P-wave (V_P) and (c) S-wave (V_S) velocity of Rw90 at high *P-T* conditions from this study, plotted with 2σ error bars. The solid curves are calculated along isotherms using the fitted finite-strain EoS model as described in the text, with shaded regions representing 95% confidence intervals. All curves and symbols are color-coded according to temperature, with the color scale shown on the right. The error bars for the volumes are within the size of the symbols. (d) The residuals between the model calculation and experimental data for V, V_P, and V_S are plotted as relative percentage deviations from the model predictions.

trend. This is illustrated in Fig. 1a, which shows a pressure drop from 9.4 to 7.1 GPa (with no intermediate data) resulting from the blow-out.

The *PVT*-velocity data were combined and fitted to a finite-strain EoS using the thermodynamically self-consistent Mie–Debye–Grüneisen Birch–Murnaghan formalism (Stixrude and Lithgow-Bertelloni, 2005), as implemented within the BurnMan software package (Cottaar et al., 2014; Myhill et al., 2023). In order not to overly bias fit parameters to the diffraction data, which are far more numerous than velocity measurements, these were subsampled in collection order at a rate of 1 in every 100 data. The best fit EoS parameters obtained were V_0= 39.69(2) cm^3/mol, $K_0 = 183(4)$ GPa, $K_0' = 5.5(3)$, $G_0 = 125(2)$ GPa, $G_0' = 1.3(1)$, $q_0 = 0.3(3)$, $\gamma_0 = 1.27(4)$, $\theta_0 = 1100(100)$ K and η_{S0}= 3.5(2). Here, V_0 is the molar volume; K_0 and K_0' are the isothermal bulk modulus and its pressure derivative; G_0 and G_0' are the shear modulus and its pressure derivative; γ_0 is the Grüneisen parameter; θ_0 is the Debye temperature; and q_0 and η_{S0} are the logarithmic volume and shear strain derivatives of the Grüneisen parameter, respectively. The resulting fit is plotted as solid curves in Fig. 1 with 95% confidence intervals indicated by the shaded regions. As expected, most of the experimental data falls within the 95% confidence intervals. The mismatch between the model calculations and experimental data, shown as the relative percentage difference, is plotted in Fig. 1d. $\Delta V/V$ is less than 0.3% and $\Delta V_P/V_P$ and $\Delta V_S/V_S$ are less than 0.8% for all data. The slightly larger deviation in volumes between 11 and 12 GPa (Fig. 1d) may have been caused by a component of non-uniform decompression (displacement of the outer anvils), leading to increased deviatoric stress at room temperature before annealing. However, a similar anomalous deviation was not observed in the measured velocities.

3.2. Comparison with previous published studies

Molar volume and velocity data from this study are compared with literature data along several isotherms in Fig. 2. For clarity, we only plot data from previous studies that report similar Fe (Fe/[Mg+Fe] = 0.1 ± 0.02) and H_2O (*i.e.* nominally dry or < 0.25 wt.%) content for comparison (Higo et al., 2008; Nishihara et al., 2004; Schulze et al., 2018; Sinogeikin et al., 2003; Zhou et al., 2022). Reported pressures from all previous studies have been converted to use the same pressure scale as this study to ensure self-consistency (Dorogokupets and Dewaele, 2007). Measured molar volumes from all studies show good agreement at all pressure and temperatures (Fig. 2a). However, the V_P (Fig. 2b) and V_S (Fig. 2c) values from this study are approximately 2.5% and 1.5% higher, respectively, than those from previous studies of nominally similar samples at 300 K. While this difference persists to high temperatures for V_P (Fig. 2b), the discrepancy with previous data for V_S decreases with increasing temperature and appears to converge at temperatures above 1500 K (Fig. 2c). Apart from the differences in absolute velocities described above, our V_P also exhibits a stronger pressure dependence at 300 K compared to previous studies, whereas V_S shows a pressure dependence consistent with earlier findings.

Whilst the offset to faster velocity measurements at 300 K from previous studies might initially suggest a problem with the data presented here, there are several differences between present and previous studies that together may explain this offset.

(1) Variations of H_2O content, which is known to reduce velocities, exist between the samples from the different studies. Our sample contains 0.003–0.035 wt.% H_2O as determined by FTIR. This is significantly lower than the sample studied by Schulze et al. (2018). The H_2O content of the samples used by Higo et al. (2008) and Sinogeikin et al. (2003) were not measured, but assumed by the authors to be negligible. The water content in the sample of Zhou et al. (2022) was reported to be zero. However, this seems inconsistent as their synthesized crystals are typically 30–90 μm whereas our samples grown for the same temperature and half of the time, have a grain size that is ubiquitously < 10 μm. We respectively suggest that Zhou et al. (2022) may have underestimated the water content of their sample, possibly because their samples are very small (maximum 50 μm thick and 90 μm diameter) and the FTIR detection limits are significantly higher than measurements in this study (polycrystalline wafer of 228 μm thickness measured using a 300 μm square aperture). However, this cannot be critically assessed because the reported FTIR spectra (Figure S1 in Zhou et al., 2022) is background corrected, has low vertical scale resolution, and is only shown from 2400 to 3800 cm^{-1}. Considering these comparisons, it is very possible that our samples are the driest of all those investigated to date, and thus expected to have the highest velocities. Added to this, there are at least four water-incorporation mechanisms in Rw (Grüninger et al., 2017, 2020; Thomson et al., 2021), which may each have different effects on elasticity. However, we acknowledge that the velocity increase cannot solely be explained by lower water contents. V_P and V_S in our study are observed to be ~0.2 km·s^{-1} or ~0.1 km·s^{-1} faster than Schulze et al. (2018) which implies our sample should have between 0.4–0.5 wt.% and 1–1.67 wt.% less water than Schulze et al. (2018), depending on what the effect of water is on velocities actually is (Mao et al., 2012; Schulze et al., 2018). So water content alone can at best explain about 50% of the velocities differences observed in this

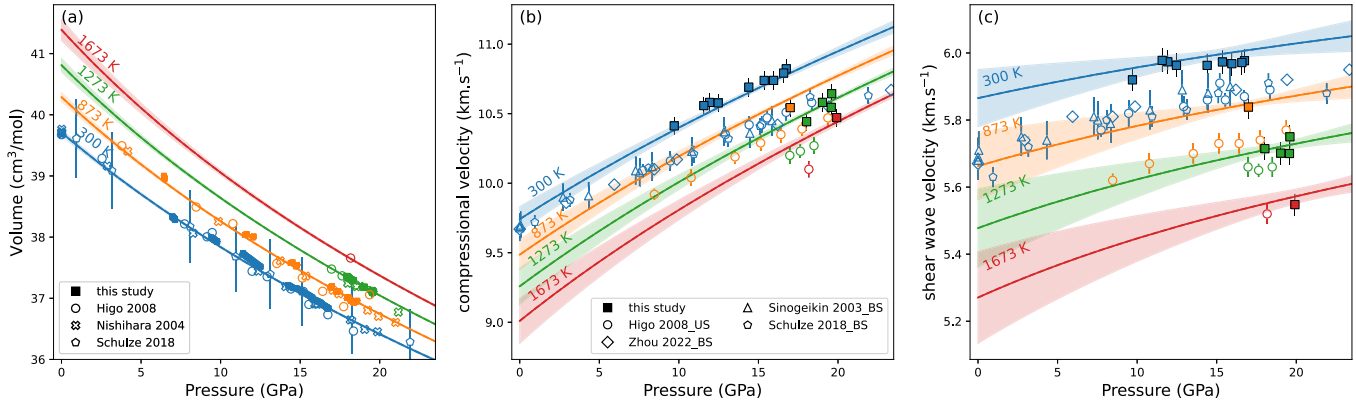

Fig. 2. Comparison of (a) volume (V), (b) P-wave (V_P) and (c) S-wave (V_S) velocities of Rw90 from our EoS with previous studies as a function of pressure along several chosen isothermal temperatures. The solid symbols are from this study, whilst open symbols are from previous studies on nominally dry Rw90 (Higo et al., 2008, Mg#91; Nishihara et al., 2004, Mg#90.7; Schulze et al., 2018, Mg#88.5, 0.21% H_2O, Fe^{3+}/Fe^{tot} = 0.15–0.19; Sinogeikin et al., 2003, Mg#91.4; Zhou et al., 2022, Mg#90.4, 0% H_2O). Only data within ± 25 K of isotherms, plotted as solid curves with shaded regions representing 95% confidence intervals, are shown. Error bars are 1σ and are within the size of the symbols if not apparent.

study, but nevertheless, when added to other factors below, it may be an important contributor.

(2) Differences in the ferric iron content of Rw samples may also partially explain the observed velocity offset. Whilst the exact impact of Fe^{3+} on the Rw velocity remains uncertain, it is known that ferric iron incorporation is associated with increased defect concentrations and/or cation disorder (Mrosko et al., 2013; Thomson et al., 2021), which in turn are known to reduce the sound velocities of Rw (Panero, 2010). Of the studies compared, only Schulze et al. (2018) reported the ferric/total iron content, which was 0.15. This is three times more enriched in ferric iron than our study ($Fe^{3+}/\sum Fe = 0.056 \pm 0.012$). Samples from Schulze et al. (2018) must have contained more defects/disorder, and therefore should have inherently lower velocities.

(3) The small variations in total iron contents (*i.e.* Schulze et al., 2018 studied a Mg# 89 Rw) also affect velocities. Based on previous data a 2% increase in Fe content increases V_P and V_S by ~0.056 and 0.046 km·s^{-1} respectively at ~15 GPa and 300 K (Higo et al., 2006).

(4) It is possible that intrinsic differences between the experimental techniques in different studies also contribute to the reported differences. While Higo et al. (2008) employed ultrasonic interferometry with samples fully annealed at high *PT* conditions, Sinogeikin et al. (2003), Schulze et al. (2018) and Zhou et al. (2022) are single-crystal Brillouin scattering measurements and inferred polycrystalline velocities via the Voigt-Reuss-Hill averaging scheme. Fundamentally, ultrasonic experiments make velocity measurements immediately after high temperature stress relaxation. In contrast, Brillouin measurements were collected during compression without high temperature annealing using methanol–ethanol–water (16:3:1) (Sinogeikin et al., 2003) or Neon (Schulze et al., 2018; Zhou et al., 2022) as a pressure transmitting medium. Whilst Neon remains approximately hydrostatic to ~ 15 GPa, methanol–ethanol–water ceases to be hydrostatic at ~ 9 GPa (Klotz et al., 2009). We are unaware of any systematic investigation of whether Brillouin and ultrasonic velocity measurements suffer from systematic offsets.

(5) Differences in the systematic experimental uncertainties between this and the previous ultrasonic measurements (*i.e.* Higo et al., 2008) can contribute to the apparent offset with this study. For instance, in the study of Higo et al. (2008) it is unclear whether any corrections were made for the travel time due to the gold marker foils (*e.g.* Noda et al., 2022). Whilst we cannot rigorously evaluate such corrections due to insufficient information provided, true velocities could be up to 1% faster than reported. In addition, Higo et al. (2008) studied a significantly longer sample (~1.5 mm *vs* ~0.55 mm in this study) which must have experienced a larger thermal gradient compared with this study which would alter the apparent temperature dependence of velocities.

So while we admit that we cannot unambiguously explain the velocity offset, the combination of lower water concentration, ferric/ferrous ratio, iron content and defects, and different experimental procedures can account for one to two percent differences in velocities. Indeed, ambient temperature velocities of similar composition iron bearing Rw containing 1–1.1 wt.% water vary by 2–4% (Fig. S10), so the offset seen in this study is not abnormal. The fact that our measured velocities are highest is consistent with our sample being demonstrably dry and having very low ferric iron and related defect concentrations.

4. Discussion

4.1. Temperature effect on sound velocities of Rw

The 520 km and 660 km seismic discontinuities are assumed to be associated with the phase transformation of $(Mg,Fe)_2SiO_4$ wadsleyite to Rw and the breakdown of Rw to bridgmanite + ferropericlase, respectively. The depth and magnitude of these discontinuities, as well as seismic anomalies, vary globally, which presumably reflect chemical and thermal heterogeneities within the MTZ (*e.g.* Jenkins et al., 2016). Such variations are widely used to estimate the water content and temperature anomalies in the MTZ based on experimental and theoretical studies of the effect of water, temperature and iron content on discontinuity depth, which include constraints on the sound velocities of Rw.

However, the estimated water content and temperature anomalies in the MTZ vary between different studies (Houser, 2016; Inoue et al., 2010; Jacobsen and Smyth, 2006; Mao et al., 2012; Schulze et al., 2018; Suetsugu et al., 2006; Wang et al., 2021; Zhou et al., 2022), probably due to the different velocity temperature dependencies used by the different studies. Since most previous measurements of Rw's sound velocities are limited to temperatures < 700 K (Mao et al., 2012; Sinogeikin et al., 2003; Zhou et al., 2022), the extensive extrapolations to MTZ temperatures (~1800 K) may also introduce large uncertainties.

Fig. 3 shows the temperature dependence of V_P and V_S for nominally anhydrous Rw90 at ~19 GPa, based on data from this study alongside that of previous work. Elastic model calculations from different studies are also plotted as solid and dashed curves for comparison. The trend of both V_P and V_S from Higo et al. (2008) agrees fairly well with the current study (dV_P/dT and dV_S/dT both ~−0.35 m·s^{-1}·K^{-1}) across the entire temperature range. In contrast, Zhou et al. (2022) observed a much smaller temperature effect on sound velocity (dV_P/dT ~−0.18 and dV_S/dT ~−0.16 m·s^{-1}·K^{-1} respectively), as do ab initio calculations (Núñez Valdez et al., 2012). While both Higo et al. (2008) and this study have measured the sound velocities of Rw90 at high pressures and temperatures up to 1650 K, the measurements from Zhou et al. (2022) only extend to 700 K, suggesting that extrapolation may significantly underestimate the velocity reduction caused by temperature conditions that exist at actual MTZ conditions. These insights emphasize the necessity of measuring mineral properties under relevant mantle conditions or as close to these as possible, rather than relying solely on extrapolations or *ab initio* theory. We observe that at 19 GPa and 1800 K, an increase in temperature of 100 K reduces V_P and V_S by 0.045 km/s (0.5%) and 0.042 km/s (0.7%), respectively. These temperature derivatives are significantly larger than those used in Wang et al. (2021) (0.025 km/s for V_P and 0.014 km/s for V_S per 100 K) and reported by Zhou et al. (2022) to infer water concentrations and temperature anomalies in the MTZ. Underestimating the effect of temperature would lead to an overestimation of MTZ water content. We emphasize that, to gain a comprehensive understanding of seismic observations, it is imperative to measure the combined effects of water, Fe content (and speciation), and temperature on the sound velocities of Rw under conditions that correspond to the actual mantle.

4.2. Comparison with seismic reference models

We use our newly parameterized Rw90 elasticity model, in combination with similar model parameterizations for other major mantle minerals from Stixrude and Lithgow-Bertelloni (2024), to calculate one-dimensional seismic wave velocity profiles for pyrolite and harzburgite assemblages within the MTZ and uppermost lower mantle. The starting bulk compositions for pyrolite and harzburgite were taken from Xu et al. (2008) (Table S4). For pyrolite, a bulk oxygen content similar to that of the upper mantle (*i.e.* $Fe^{3+}/Fe = 0.03$) is assumed (Canil and O'Neill, 1996). Equilibrium phase proportions (Table S5–S6) and compositions (Table S7–S8) are calculated using Gibbs-free energy minimization with Perple_X 7.1.13 (Connolly, 2005) along the geotherm from Brown and Shankland (1981), employing the database from Stixrude and Lithgow-Bertelloni (2024). Results show that, in the middle MTZ, pyrolite consists of ~60 vol.% Rw90 and ~40 vol.% garnet. The proportion of garnet gradually decreases with depth as Ca-perovskite exsolves prior to the later transformation to bridgmanite. After the

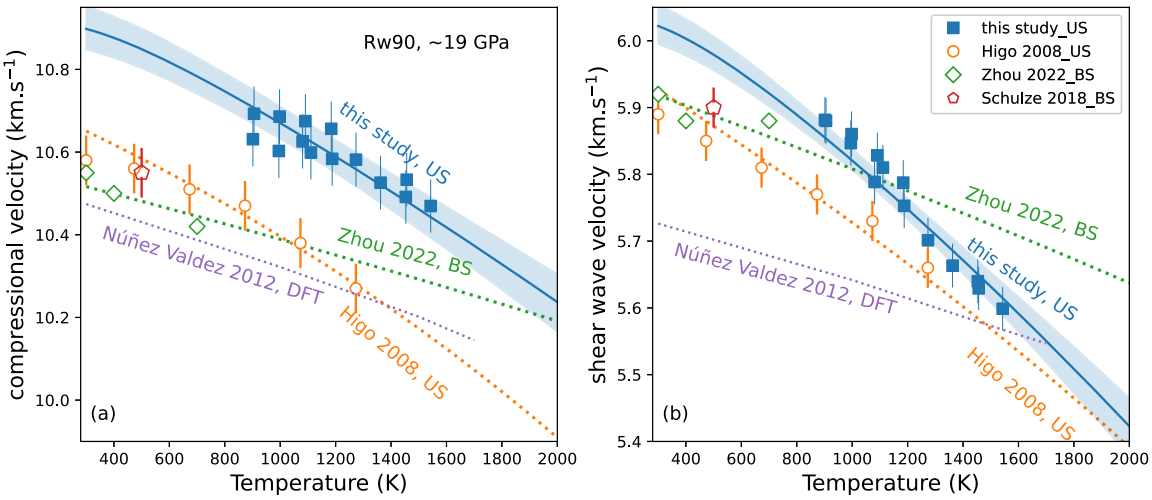

Fig. 3. (a) P-wave (V_P) and (b) S-wave (V_S) velocity of nominally dry Rw90 plotted against temperature at 19 GPa. Solid symbols are data from this study, open symbols are from previous ultrasonic interferometry (Higo et al., 2008) and Brillouin scattering (Schulze et al., 2018; Zhou et al., 2022) studies. The curves represent model calculations from corresponding studies. The first-principles calculation result from Núñez Valdez et al. (2012), which are for dry Mg# 87.5 Rw, are shown for comparison. Error bars are 1σ and are within the size of the symbols if not apparent.

post-spinel transition, pyrolite in the topmost lower mantle consists of ~75 vol.% bridgmanite, ~18 vol.% ferropericlase, and ~7 vol.% Ca perovskite, along with a small amount of Fe metal (Table S5) produced by disproportionation reactions (Frost et al., 2004; Huang et al., 2021). The depleted harzburgite assemblage consists of ~80 vol.% Rw and ~20 vol.% garnet in the middle MTZ, becoming an assemblage of ~74 vol.% bridgmanite, ~25 vol.% ferropericlase and ~ 1 vol.% Ca perovskite in the lower mantle (Table S6). These results generally align with previous experimental observations (Irifune, 1994; Irifune et al., 2010; Ishii et al., 2018, 2019).

The seismic wave velocities of pyrolite and harzburgite were then calculated along the geotherm using the thermodynamic formalism of Stixrude and Lithgow-Bertelloni (2005), implemented in the BurnMan package (Cottaar et al., 2014; Myhill et al., 2023). The Reuss average was used to calculate the elastic moduli of each mineral solution, and the Voigt–Reuss–Hill average was applied to derive the elasticity of each rock aggregate. Uncertainties in the predicted bulk rock velocity profiles are estimated to be ~0.5% for V_P and ~1% for V_S at any specific depth, assuming that the uncertainties in the predictions using parameters from Stixrude and Lithgow-Bertelloni (2024) (Table S9) are comparable to those observed for Rw in this study.

Fig. 4 compares the predicted sound velocity and density profiles of pyrolite and harzburgite assemblages with the seismic reference models PREM (Dziewonski and Anderson, 1981) and AK135 (Kennett et al., 1995). The estimated V_P of pyrolite (red curve, Fig. 4a) agrees well with PREM in the middle to lower part of the MTZ and the uppermost lower mantle, however the overall velocity increase is spread over a large pressure interval. This is because the dissociation reaction of Rw → bridgmanite + ferropericlase itself results in a V_P increase that is much too small, and so the transition is dominated by the garnet transition

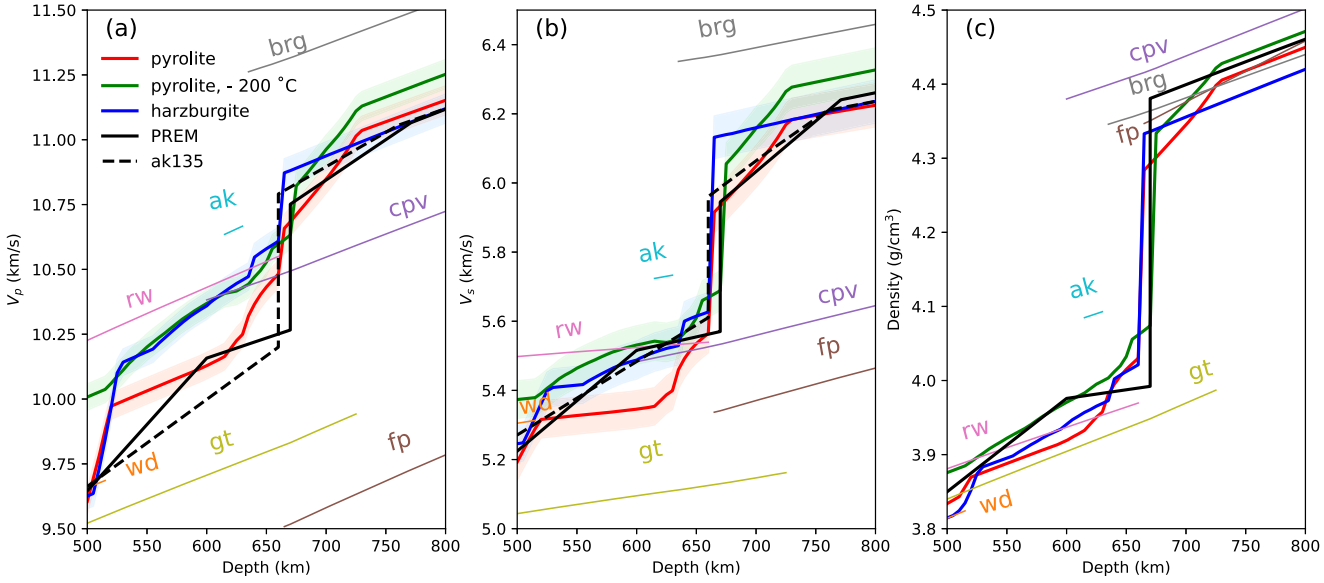

Fig. 4. Comparison of (a) P-wave (V_P) and (b) S-wave (V_S) velocities and (c) density of pyrolite and harzburgite compositions with two seismological models, PREM (Dziewonski and Anderson, 1981) and AK135 (Kennett et al., 1995). The red and blue solid curves represent the calculated results for pyrolite and harzburgite, respectively, along the geotherm of Brown and Shankland (1981), with the shaded areas indicating an estimated uncertainty of ~1%. The velocities and densities of relevant high-pressure phases are also shown for comparison. wd: wadsleyite; rw: ringwoodite; gt: majorite garnet; ak: akimotoite; cpv: Ca perovskite; brg: bridgmanite; fp: ferropericlase.

which occurs over a wide pressure range. Pyrolite is, thus, unable to produce the large and sharp discontinuity at 660 km seen in both seismic reference models. There is also a mismatch in the 650–730 km depth range due to the gradual transformation of majorite garnet to bridgmanite and calcium perovskite.

Conversely, V_S for a pyrolite assemblage agrees very well with the seismic models in the uppermost lower mantle just below 660 km, with a discontinuity magnitude at 660 km that is consistent with seismological observations. However, the V_S of pyrolite in the bottom 150 km of the MTZ is about 0.2 km/s lower than seismic observations. Moreover, the predicted density in the lower MTZ and the density jump at 660 km for pyrolite are lower compared to the PREM model. In our modelling, the transformation of majorite garnet to bridgmanite in pyrolite occurs over a pressure range from 22.4 GPa to 26.5 GPa. If this transition were to occur over a narrower pressure range, the V_P and density discontinuities at 660 km would be larger, more closely matching seismic observations. However, the V_S jump would then be too large and inconsistent with seismic observations. Therefore, our results indicate that a standard dry pyrolite assemblage provides a poor match to seismic reference models along a normal mantle geotherm at the base of the MTZ and topmost lower mantle (Dziewonski and Anderson, 1981; Kennett et al., 1995), and in particular cannot produce the sharp jump in V_P required by seismology.

Similar discrepancies between the predictions of mineralogical models and seismic observations have also been reported previously (Gréaux et al., 2019; Irifune et al., 2008; Xu et al., 2008), leading to suggestions that material chemically distinct from normal pyrolite may be present in the MTZ. Since tomographic observations reveal that some subducting slabs stagnate and accumulate in the MTZ (Agrusta et al., 2017; Fukao and Obayashi, 2013; Van der Hilst et al., 1997), and since they consist of mid-ocean ridge basalt (MORB) and underlying harzburgite, these assemblages have been suggested as potential MTZ candidates (Gréaux et al., 2019; Irifune et al., 2008; Ishii et al., 2019; Pamato et al., 2016; Xu et al., 2008). However, neither harzburgite nor MORB can explain all the observed discrepancies between mineralogical predictions and seismic observations. A harzburgite mineral assemblage, characterized by higher Rw and lower majorite garnet proportions, alongside the presence of akimotoite, appears to better match V_S in the MTZ (blue curves in Fig. 4b). Additionally, the lower Al content in majorite garnet within harzburgite leads to its transformation to bridgmanite over a narrower pressure range, offering a better match for V_P between 660 and 750 km depths. However, the predicted V_P of harzburgite is significantly higher than seismic observations in the lower MTZ, and its V_S is too high in the topmost lower mantle. In addition, the density of harzburgite is insufficient in the lower MTZ. On the other hand, the velocities of MORB are even slower than those of pyrolite (Gréaux et al., 2019) due to the high proportion of majorite garnet, which has low seismic velocities among the potential minerals. To increase the V_S and density of pyrolite in the lower MTZ to match seismic models, one potential explanation is that temperatures may be lower than the predicted geotherm. Decreasing temperature would generally increase the sound velocity and density of minerals. In the case of pyrolite, a temperature profile 200 K lower than the geotherm would also facilitate the formation of akimotoite at the base of MTZ, thereby further enhancing the sound velocity of the bulk rock. As shown in Fig. 4 (green curves), this 200 K temperature reduction raises the predicted V_S and density models to match seismic reference models. However, it results in a V_P that is too high in the lower MTZ and a V_P jump that remains too low at the 660 km discontinuity.

However, it is important to acknowledge the inherent uncertainties in both the seismic models and thermodynamic calculations. 1D seismic reference models represent globally averaged velocity structures, which are not uniquely determined and involve tradeoffs between discontinuity magnitudes and velocity gradients. In most reference models, the underlying structure is described using polynomial functions, which lack direct theoretical justification (Frost, 2008). On the other hand, the thermo-elastic properties of many relevant minerals, essential for estimating the velocities of bulk rock compositions, remain poorly constrained. To date, the elasticities of iron-bearing ferropericlase, akimotoite and bridgmanite with expected mantle compositions have yet to be measured under high *P-T* conditions comparable to those of the MTZ or uppermost lower mantle. Moreover, although the elasticities of some majorite garnet endmembers (majorite, pyrope, grossular, and almandine), as well as majorite garnet with either a complex "natural" chemistry or an 80% majorite–20% pyrope composition, have been measured under high *P-T* conditions close to those of the MTZ, each composition has only been studied once (Arimoto et al., 2015; Chantel et al., 2016; Irifune et al., 2008; Kono et al., 2010; Liu et al., 2015; Zhou et al., 2021). With no data available for Na-majorite or andradite garnet, the overall database remains incomplete. Although many *ab initio* estimates exist for mantle mineral properties and serve as excellent starting points in the absence of experimental data, they typically require small corrections in volume and moduli (*i.e.* Zhang et al., 2013) to match experimental findings. While these corrections are usually minor (a few percent in volume), their accuracy at high *P-T* conditions cannot be reliably assessed without experimental data.

Additionally, compositional changes in minerals are taken into account in this study, as different endmembers may contribute differently to the elasticity of a solid solution. For instance, majorite garnet begins to exsolve Ca-perovskite at ~18 GPa and undergoes a gradual phase transition to bridgmanite at the base of the MTZ and the top of the lower mantle (Irifune, 1994; Ishii et al., 2018; Saikia et al., 2008). During this transition, the majorite and grossular components in garnet decrease, while the pyrope component increases (Pamato et al., 2016; Saikia et al., 2008). Simultaneously, Al content in bridgmanite gradually increases within the top 50 km of the lower mantle, resulting in higher Fe^{3+} content in bridgmanite (Huang et al., 2021; Irifune, 1994; Ishii et al., 2018). Although thermodynamic models are employed to account for these compositional changes, further experimental studies under relevant mantle conditions are necessary to validate these predictions and better constrain the bulk composition of the deep mantle. And finally, the bulk chemistry of mantle assemblages may exhibit variations that are not fully captured by current models, due to the simplification of assigning a single chemistry and the limitations of thermodynamic models in a simplified chemical system.

5. Conclusions

We have investigated the elastic properties of nominally dry (0.003–0.035 wt.% H_2O) $(Mg_{0.91}Fe_{0.09})_2SiO_4$ ringwoodite at high pressure and temperature conditions up to 21 GPa and 1650 K using ultrasonic interferometry combined with synchrotron X-radiation in the multi-anvil press. V_P and V_S were found to be 2.5% and 1.5% higher than previous studies at 300 K and high pressure, respectively. This offset can be explained by a combination of variable water concentration, iron content, iron speciation and experimental techniques compared with previous studies. While this discrepancy in V_P persists to high temperatures, V_S becomes consistent with previous measurements above 1500 K. A global fit of the measured *PVT*-velocity data gives V_0= 39.69(2) cm^3/mol, $K_0 = 183(4)$ GPa, $K_0' = 5.5(3)$, $G_0 = 125(2)$ GPa, $G_0' = 1.3(1)$, $q_0 = 0.3(3)$, $\gamma_0 = 1.27(4)$, $\theta_0 = 1100(100)$ K and η_{S0}= 3.5(2). Using these parameters and the parameters of other major mantle minerals from literature models, we predict the sound velocities for pyrolite and harzburgite bulk compositions along the mantle geotherm. Our results show that "dry" pyrolite, which contains ~60 vol.% ringwoodite, cannot satisfy the magnitude and sharpness of the V_P velocity jumps at the 660 km discontinuity as required by seismology.

CRediT authorship contribution statement

Rong Huang: Writing – original draft, Visualization, Methodology, Investigation, Formal analysis, Data curation, Conceptualization.

Andrew R. Thomson: Writing – review & editing, Supervision, Resources, Methodology, Investigation, Funding acquisition, Conceptualization. **John P. Brodholt:** Writing – review & editing, Supervision, Investigation, Funding acquisition, Conceptualization. **Wilson A. Crichton:** Writing – review & editing, Methodology, Investigation. **Anja Rosenthal:** Writing – review & editing, Investigation. **Dmitrii Druzhbin:** Investigation. **Nicholas Backhouse:** Investigation. **Isaac Taschimowitz:** Investigation. **Dimitrios Bessas:** Investigation. **Sergey Yaroslavtsev:** Investigation. **Biao Wang:** Investigation.

Declaration of competing interest

The authors declare that they have no known competing financial interests or personal relationships that could have appeared to influence the work reported in this paper.

Acknowledgments

We would like to thank David Dobson for the insightful discussion on sample length determination, Ian Wood for his assistance with X-ray diffraction measurements, and Fang Xu for providing San Carlos olivine powders. This work was supported by the UKRI grant NE/T007737/1.

Supplementary materials

Supplementary material associated with this article can be found, in the online version, at doi:10.1016/j.epsl.2025.119416.

Data availability

Data will be made available on request.

References

Agrusta, R., Goes, S., Van Hunen, J., 2017. Subducting-slab transition-zone interaction: stagnation, penetration and mode switches. Earth Planet. Sci. Lett. 464, 10–23. https://doi.org/10.1016/j.epsl.2017.02.005.

Arimoto, T., Gréaux, S., Irifune, T., Zhou, C., Higo, Y., 2015. Sound velocities of $Fe_3Al_2Si_3O_{12}$ almandine up to 19 GPa and 1700 K. Phys. Earth Planet. Inter. 246, 1–8. https://doi.org/10.1016/j.pepi.2015.06.004.

Brown, J., Shankland, T., 1981. Thermodynamic parameters in the Earth as determined from seismic profiles. Geophys. J. Int. 66, 579–596. https://doi.org/10.1111/j.1365-246X.1981.tb04891.x.

Canil, D., O'Neill, H.S.C, 1996. Distribution of ferric iron in some upper-mantle assemblages. J. Petrol. 37, 609–635. https://doi.org/10.1093/petrology/37.3.609.

Chantel, J., Manthilake, G.M., Frost, D.J., Beyer, C., Boffa Ballaran, T., Jing, Z., Wang, Y., 2016. Elastic wave velocities in polycrystalline $Mg_3Al_2Si_3O_{12}$-pyrope garnet to 24 GPa and 1300 K. Am. Mineral. 101, 991–997. https://doi.org/10.2138/am-2016-5335.

Collins, T.J., 2007. ImageJ for microscopy. BioTechniques 43, S25–S30. https://doi.org/10.2144/000112517.

Connolly, J.A., 2005. Computation of phase equilibria by linear programming: a tool for geodynamic modeling and its application to subduction zone decarbonation. Earth Planet. Sci. Lett. 236, 524–541. https://doi.org/10.1016/j.epsl.2005.04.033.

Cottaar, S., Heister, T., Rose, I., Unterborn, C., 2014. BurnMan: a lower mantle mineral physics toolkit. Geochem. Geophys. Geosyst. 15, 1164–1179. https://doi.org/10.1002/2013GC005122.

Crichton, W.A., Kieffer, J., Wattecamps, P., Valls, V., Berruyer, G., Ruat, M., Favre-Nicolin, V., 2023. Correction and integration of solid-angle data from the azimuthally resolving 2D detector at ID06-LVP, ESRF. J. Synchrotron Radiat. 30. https://doi.org/10.1107/S1600577523008020.

Crichton, W.A., Thomson, A.R., Rosenthal, A., Spektor, K., Druzhbin, D., Winkler, B., et al., 2024. EBS status of the large-volume press at beamline ID06-LVP. High Press Res 1–31. https://doi.org/10.1080/08957959.2024.2379354.

Dorogokupets, P., Dewaele, A., 2007. Equations of state of MgO, Au, Pt, NaCl-B1, and NaCl-B2: internally consistent high-temperature pressure scales. High Press. Res. 27, 431–446. https://doi.org/10.1080/08957950701659700.

Dziewonski, A.M., Anderson, D.L., 1981. Preliminary reference Earth model. Phys. Earth Planet. Inter. 25, 297–356. https://doi.org/10.1016/0031-9201(81)90046-7.

Fei, H., Katsura, T., 2020. High water solubility of ringwoodite at mantle transition zone temperature. Earth Planet. Sci. Lett. 531, 115987. https://doi.org/10.1016/j.epsl.2019.115987.

Fei, H., Katsura, T., 2021. Water solubility in Fe-bearing wadsleyite at mantle transition zone temperatures. Geophys. Res. Lett. 48, e2021GL092836.

Frost, D.J., 2008. The upper mantle and transition zone. Elements 4, 171–176. https://doi.org/10.2113/gselements.4.3.171.

Frost, D.J., Liebske, C., Langenhorst, F., McCammon, C.A., Trønnes, R.G., Rubie, D.C., 2004. Experimental evidence for the existence of iron-rich metal in the Earth's lower mantle. Nature 428, 409–412. https://doi.org/10.1038/nature02413.

Fukao, Y., Obayashi, M., 2013. Subducted slabs stagnant above, penetrating through, and trapped below the 660 km discontinuity. J. Geophys. Res.: Solid Earth 118, 5920–5938. https://doi.org/10.1002/2013JB010466.

Gréaux, S., Irifune, T., Higo, Y., Tange, Y., Arimoto, T., Liu, Z., Yamada, A., 2019. Sound velocity of $CaSiO_3$ perovskite suggests the presence of basaltic crust in the Earth's lower mantle. Nature 565, 218–221. https://doi.org/10.1038/s41586-018-0816-5.

Grüninger, H., Armstrong, K., Greim, D., Boffa-Ballaran, T., Frost, D.J., Senker, J.r., 2017. Hidden oceans? Unraveling the structure of hydrous defects in the Earth's deep interior. J. Am. Chem. Soc. 139, 10499–10505. https://doi.org/10.1021/jacs.7b05432.

Grüninger, H., Liu, Z., Brauckmann, J.O., Fei, H., Ballaran, T.B., Martin, T., et al., 2020. Hydroxyl defects and oxide vacancies within ringwoodite—Toward understanding the defect chemistry of spinel-type oxides. J. Phys. Chem. C 124, 12001–12009. https://doi.org/10.1021/acs.jpcc.0c03016.

Higo, Y., Inoue, T., Irifune, T., Funakoshi, K.-i., Li, B., 2008. Elastic wave velocities of $(Mg_{0.91}Fe_{0.09})_2SiO_4$ ringwoodite under P–T conditions of the mantle transition region. Phys. Earth Planet. Inter. 166, 167–174. https://doi.org/10.1016/j.pepi.2008.01.003.

Higo, Y., Inoue, T., Li, B., Irifune, T., Liebermann, R.C., 2006. The effect of iron on the elastic properties of ringwoodite at high pressure. Phys. Earth Planet. Inter. 159, 276–285. https://doi.org/10.1016/j.pepi.2006.08.004.

Houser, C., 2016. Global seismic data reveal little water in the mantle transition zone. Earth Planet. Sci. Lett. 448, 94–101. https://doi.org/10.1016/j.epsl.2016.04.018.

Huang, R., Boffa Ballaran, T., McCammon, C.A., Miyajima, N., Dolejš, D., Frost, D.J., 2021. The composition and redox state of bridgmanite in the lower mantle as a function of oxygen fugacity. Geochim. Cosmochim. Acta 303, 110–136. https://doi.org/10.1016/j.gca.2021.02.036.

Inoue, T., Wada, T., Sasaki, R., Yurimoto, H., 2010. Water partitioning in the Earth's mantle. Phys. Earth Planet. Inter. 183, 245–251. https://doi.org/10.1016/j.pepi.2010.08.003.

Irifune, T., 1994. Absence of an aluminous phase in the upper part of the Earth's lower mantle. Nature 370, 131–133. https://doi.org/10.1038/370131a0.

Irifune, T., Higo, Y., Inoue, T., Kono, Y., Ohfuji, H., Funakoshi, K., 2008. Sound velocities of majorite garnet and the composition of the mantle transition region. Nature 451, 814–817. https://doi.org/10.1038/nature06551.

Irifune, T., Shinmei, T., McCammon, C.A., Miyajima, N., Rubie, D.C., Frost, D.J., 2010. Iron partitioning and density changes of pyrolite in Earth's lower mantle. Science 327, 193–195. https://doi.org/10.1126/science.1181443.

Ishii, T., Kojitani, H., Akaogi, M., 2018. Phase relations and mineral chemistry in pyrolitic mantle at 1600–2200 °C under pressures up to the uppermost lower mantle: phase transitions around the 660-km discontinuity and dynamics of upwelling hot plumes. Phys. Earth Planet. Inter. 274, 127–137. https://doi.org/10.1016/j.pepi.2017.10.005.

Ishii, T., Kojitani, H., Akaogi, M., 2019. Phase relations of harzburgite and MORB up to the uppermost lower mantle conditions: precise comparison with pyrolite by multisample cell high-pressure experiments with implication to dynamics of subducted slabs. J. Geophys. Res.: Solid Earth 124, 3491–3507. https://doi.org/10.1029/2018JB016749.

Jacobsen, S.D., Smyth, J.R., 2006. Effect of water on the sound velocities of ringwoodite in the transition zone. Earth's deep water cycle 168, 131–145. https://doi.org/10.1029/168GM10.

Jacobsen, S.D., Smyth, J.R., Spetzler, H., Holl, C.M., Frost, D.J., 2004. Sound velocities and elastic constants of iron-bearing hydrous ringwoodite. Phys. Earth Planet. Inter. 143-144, 47–56. https://doi.org/10.1016/j.pepi.2003.07.019.

Jenkins, J., Cottaar, S., White, R., Deuss, A., 2016. Depressed mantle discontinuities beneath Iceland: evidence of a garnet controlled 660 km discontinuity? Earth Planet. Sci. Lett. 433, 159–168. https://doi.org/10.1016/j.epsl.2015.10.053.

Kennett, B.L., Engdahl, E., Buland, R., 1995. Constraints on seismic velocities in the Earth from traveltimes. Geophys. J. Int. 122, 108–124. https://doi.org/10.1111/j.1365-246X.1995.tb03540.x.

Klotz, S., Chervin, J.C., Munsch, P., Le Marchand, G., 2009. Hydrostatic limits of 11 pressure transmitting media. J. Phys. D Appl. Phys. 42, 075413. https://doi.org/10.1088/0022-3727/42/7/075413.

Kono, Y., Gréaux, S., Higo, Y., Ohfuji, H., Irifune, T., 2010. Pressure and temperature dependences of elastic properties of grossular garnet up to 17 GPa and 1 650 K. J. Earth Sci. 21, 782–791. https://doi.org/10.1007/s12583-010-0112-2.

Kurnosov, A., Marquardt, H., Frost, D.J., Boffa Ballaran, T., Ziberna, L., 2017. Evidence for a Fe^{3+}-rich pyrolitic lower mantle from (Al,Fe)-bearing bridgmanite elasticity data. Nature 543, 543–546. https://doi.org/10.1038/nature21390.

Liu, Z., Irifune, T., Gréaux, S., Arimoto, T., Shinmei, T., Higo, Y., 2015. Elastic wave velocity of polycrystalline $Mj_{80}Py_{20}$ garnet to 21 GPa and 2000 K. Phys. Chem. Miner. 42, 213–222. https://doi.org/10.1007/s00269-014-0712-y.

Mao, Z., Lin, J.-F., Jacobsen, S.D., Duffy, T.S., Chang, Y.-Y., Smyth, J.R., et al., 2012. Sound velocities of hydrous ringwoodite to 16 GPa and 673 K. Earth Planet. Sci. Lett. 331, 112–119. https://doi.org/10.1016/j.epsl.2012.03.001.

Mayama, N., Suzuki, I., Saito, T., Ohno, I., Katsura, T., Yoneda, A., 2005. Temperature dependence of the elastic moduli of ringwoodite. Phys. Earth Planet. Inter. 148, 353–359. https://doi.org/10.1016/j.pepi.2004.09.007.

Meier, U., Trampert, J., Curtis, A., 2009. Global variations of temperature and water content in the mantle transition zone from higher mode surface waves. Earth Planet. Sci. Lett. 282, 91–101. https://doi.org/10.1016/j.epsl.2009.03.004.

Mrosko, M., Lenz, S., McCammon, C.A., Taran, M., Wirth, R., Koch-Müller, M., 2013. Hydrogen incorporation and the oxidation state of iron in ringwoodite: a

spectroscopic study. Am. Mineral. 98, 629–636. https://doi.org/10.2138/am.2013.4245.
Myhill R., Cottaar, S., Heister, T., Rose, I., Unterborn, C., Dannberg, J., & Gassmoeller, R. (2023). BurnMan–a Python toolkit for planetary geophysics, geochemistry and thermodynamics. https://doi.org/10.21105/joss.05389.
Nishihara, Y., Takahashi, E., Matsukage, K.N., Iguchi, T., Nakayama, K., Funakoshi, K.-i., 2004. Thermal equation of state of $(Mg_{0.91}Fe_{0.09})_2SiO_4$ ringwoodite. Phys. Earth Planet. Inter. 143, 33–46. https://doi.org/10.1016/j.pepi.2003.02.001.
Noda, M., Inoue, T., Tsuchiya, T., Higo, Y., 2022. Reassessment of a bond correction method for *in situ* ultrasonic interferometry on elastic wave velocity measurement under high pressure and high temperature. High Press Res 42, 278–293. https://doi.org/10.1080/08957959.2022.2112677.
Núñez Valdez, M., Wu, Z., Yonggang, G.Y., Revenaugh, J., Wentzcovitch, R.M, 2012. Thermoelastic properties of ringwoodite (Fex, Mg1− x) 2SiO4: its relationship to the 520 km seismic discontinuity. Earth Planet. Sci. Lett. 351, 115–122. https://doi.org/10.1016/j.epsl.2012.07.024.
Pamato, M.G., Kurnosov, A., Boffa Ballaran, T., Frost, D.J., Ziberna, L., Giannini, M., et al., 2016. Single crystal elasticity of majoritic garnets: stagnant slabs and thermal anomalies at the base of the transition zone. Earth Planet. Sci. Lett. 451, 114–124. https://doi.org/10.1016/j.epsl.2016.07.019.
Panero, W.R., 2010. First principles determination of the structure and elasticity of hydrous ringwoodite. J. Geophys. Res.: Solid Earth 115. https://doi.org/10.1029/2008JB006282.
Prescher, C., Prakapenka, V.B., 2015. DIOPTAS: a program for reduction of two-dimensional X-ray diffraction data and data exploration. High Press Res. 35, 223–230. https://doi.org/10.1080/08957959.2015.1059835.
Ringwood, A.E., 1991. Phase transformations and their bearing on the constitution and dynamics of the mantle. Geochim. Cosmochim. Acta 55, 2083–2110. https://doi.org/10.1016/0016-7037(91)90090-R.
Saikia, A., Frost, D.J., Rubie, D.C., 2008. Splitting of the 520-km seismic discontinuity and chemical heterogeneity in the mantle. Science 319, 1515–1518. https://doi.org/10.1126/science.115281.
Schulze, K., Marquardt, H., Kawazoe, T., Boffa Ballaran, T., McCammon, C., Koch-Müller, M., et al., 2018. Seismically invisible water in Earth's transition zone? Earth Planet. Sci. Lett. 498, 9–16. https://doi.org/10.1016/j.epsl.2018.06.021.
Sinogeikin, S.V., Bass, J.D., Katsura, T., 2003. Single-crystal elasticity of ringwoodite to high pressures and high temperatures: implications for 520 km seismic discontinuity. Phys. Earth Planet. Inter. 136, 41–66. https://doi.org/10.1016/S0031-9201(03)00022-0.
Smyth, J.R., Holl, C.M., Frost, D.J., Jacobsen, S.D., Langenhorst, F., McCammon, C.A., 2003. Structural systematics of hydrous ringwoodite and water in Earth's interior. Am. Mineral. 88, 1402–1407. https://doi.org/10.2138/am-2003-1001.
Stixrude, L., Lithgow-Bertelloni, C., 2005. Thermodynamics of mantle minerals—I. Physical properties. Geophys. J. Int. 162, 610–632. https://doi.org/10.1111/j.1365-246X.2005.02642.x.
Stixrude, L., Lithgow-Bertelloni, C., 2024. Thermodynamics of mantle minerals–III: the role of iron. Geophys. J. Int. 237, 1699–1733. https://doi.org/10.1093/gji/ggae126.
Suetsugu, D., Inoue, T., Obayashi, M., Yamada, A., Shiobara, H., Sugioka, H., et al., 2010. Depths of the 410-km and 660-km discontinuities in and around the stagnant slab beneath the Philippine Sea: is water stored in the stagnant slab? Phys. Earth Planet. Inter. 183, 270–279. https://doi.org/10.1016/j.pepi.2010.09.004.
Suetsugu, D., Inoue, T., Yamada, A., Zhao, D., Obayashi, M., 2006. Towards mapping the three-dimensional distribution of water in the transition zone from P-velocity tomography and 660-km discontinuity depths. Earth's deep water cycle 168, 237–249. https://doi.org/10.1029/168GM18.
Thomson, A.R., Piltz, R.O., Crichton, W.A., Cerantola, V., Ezad, I.S., Dobson, D.P., et al., 2021. Incorporation of tetrahedral ferric iron into hydrous ringwoodite. Am. Mineral. 106, 900–908. https://doi.org/10.2138/am-2021-7539.
Toby, B.H., Von Dreele, R.B., 2013. GSAS-II: the genesis of a modern open-source all purpose crystallography software package. J. Appl. Crystallogr. 46, 544–549. https://doi.org/10.1107/S0021889813003531.
Van der Hilst, R.D., Widiyantoro, S., Engdahl, E., 1997. Evidence for deep mantle circulation from global tomography. Nature 386, 578–584. https://doi.org/10.1038/386578a0.
Van der Meijde, M., Marone, F., Giardini, D., Van der Lee, S., 2003. Seismic evidence for water deep in Earth's upper mantle. Science 300, 1556–1558. https://doi.org/10.1126/science.10836.
Wang, W., Zhang, H., Brodholt, J.P., Wu, Z., 2021. Elasticity of hydrous ringwoodite at mantle conditions: implication for water distribution in the lowermost mantle transition zone. Earth Planet. Sci. Lett. 554, 116626. https://doi.org/10.1016/j.epsl.2020.116626.
Xu, F., Xie, L., Yoneda, A., Guignot, N., King, A., Morard, G., Antonangeli, D., 2020. TiC-MgO composite: an X-ray transparent and machinable heating element in a multi-anvil high pressure apparatus. High Press Res 40, 257–266. https://doi.org/10.1080/08957959.2020.1747452.
Xu, W., Lithgow-Bertelloni, C., Stixrude, L., Ritsema, J., 2008. The effect of bulk composition and temperature on mantle seismic structure. Earth Planet. Sci. Lett. 275, 70–79. https://doi.org/10.1016/j.epsl.2008.08.012.
Yaroslavtsev, S., 2023. SYNCmoss software package for fitting Mössbauer spectra measured with a synchrotron Mössbauer source. J. Synchrotron Radiat. 30, 596–604. https://doi.org/10.1107/S1600577523001686.
Yu, C., Goes, S., Day, E.A., van der Hilst, R.D., 2023. Seismic evidence for global basalt accumulation in the mantle transition zone. Sci. Adv. 9, eadg0095. https://doi.org/10.1126/sciadv.adg0095.
Zhang, Z., Stixrude, L., Brodholt, J., 2013. Elastic properties of $MgSiO_3$-perovskite under lower mantle conditions and the composition of the deep Earth. Earth Planet. Sci. Lett. 379, 1–12. https://doi.org/10.1016/j.epsl.2013.07.034.
Zhou, C., Gréaux, S., Liu, Z., Higo, Y., Arimoto, T., Irifune, T., 2021. Sound velocity of $MgSiO_3$ majorite garnet up to 18 GPa and 2000 K. Geophys. Res. Lett. 48, e2021GL093499. https://doi.org/10.1029/2021GL093499.
Zhou, W.-Y., Zhang, J.S., Huang, Q., Lai, X., Chen, B., Dera, P., Schmandt, B., 2022. High pressure-temperature single-crystal elasticity of ringwoodite: implications for detecting the 520 discontinuity and metastable ringwoodite at depths greater than 660 km. Earth Planet. Sci. Lett. 579, 117359. https://doi.org/10.1016/j.epsl.2021.117359.